Vol.4, No.3, Page 1814- 1824, 2026 https://doi.org/10.59628/jast.v4i3.2464 ISSN 2958-9568 JAST

SUN PUBLISHER

مجلة جامعة صنعاء للعلوم التطبيقية والتكنولوجيا

Sana'a University Journal of Applied Sciences and Technology

https://journals.su.edu.ye/index.php/jast/

Visible-Light Photocatalytic Enhancement in Hydrothermally Synthesized cd_1s_{1-x} Nanoparticles: Structural and Optical Characterization

H. Arhab[1] *, Shakib M. A. Alsowidy[2], Mohammed S. Qusailah[2] and A.M. Abdulkarem[1]

[1]**Department of Physics , Faculty of Education and Applied Sciences -Arhab, Sana'a University, Sana'a, Yemen,**
[2]**Department of Physics, Faculty of science, Sana'a University, Sana'a, Yemen**

*Corresponding author: arhabh54@gmail.com

Abstract

Cadmium sulfide cd_1s_{1-x} nanoparticles were synthesized using a simple and cost-effective hydrothermal method by varying the Cd:S molar ratio to investigate its effect on the photocatalytic degradation of Rhodamine B (Rh-B) in aqueous solution under simulated solar irradiation serves as a model organic pollutant. Structural and morphological characterization using XRD, SEM, and UV–Vis spectroscopy confirmed the particularity of cd_1s_{1-x} particle with good crystallinity and visible light absorption properties. The photocatalytic efficiency of the cd_1s_{1-x} nanoparticles exhibited a strong dependence on the sulfur ion concentration, indicating the critical role of precursor ratio in tuning photocatalyst performance. Among the samples, the one prepared with x= 0.3026 exhibited the highest degradation efficiency, achieving nearly complete removal of Rh-B within 73 minutes. The enhanced photocatalytic performance is attributed to the optimized particle size, which improves crystallinity and surface area, facilitating more efficient charge separation, light absorption, and separation of photogenerated charge carriers. This study highlights the crucial role of precursor composition in tailoring the structural and functional properties of cd_1s_{1-x} nanoparticles, providing a straightforward and scalable approach for developing efficient visible-light-responsive photocatalysts for environmental remediation applications.

Article Info

Keywords:
cd_1s_{1-x} nanoparticle, Energy, Environmental , remediation, Optical properties, photocatalysis.

Article History:
Received: 02-November-2025,
Revised: 23-December-2025,
Accepted: 26-December-2025,
Published: 28 March 2026.

1. INTRODUCTION

Environmental pollution and energy shortages are among the most pressing challenges to the sustainable development of human civilization [1–3]. As major contributors to environmental and water pollution, along with the scarcity of renewable energy sources, these issues demand urgent attention [3, 4].

Among various water treatment methods, semiconductor photocatalysis powered by solar energy is considered to be one of the most promising technologies because of its environmentally friendly, energy-efficient, and straightforward approach [5]. Cadmium sulfide (CdS), a semiconductor, exhibits notable photocatalytic activity and is therefore a promising material for environmental remediation and energy conversion applications [4]. In particular, CdS nanoparticle photocatalysts have garnered significant research interest [6, 7]. In recent years, CdS nanoparticles have garnered significant interest owing to their tunable band gap, strong visible-light absorption, and high surface area [7–9]. These materials are promising candidates for various applications, including photodegradation, solar cells, sensors, water splitting, and photodetectors [10–13].Their effectiveness in these applications is largely attributed to their suitable direct band gap (∼2.45 eV) [14, 15], which facilitates strong visible-light absorption and promotes high catalytic activity in various applications, including organic pollutant degradation, co_2 reduction, antibacterial action, and the development of electronic devices.

However, the optical transmittance of CdS is still not suf-

ficiently high for certain advanced optoelectronic applications, which limits its effectiveness in devices that require high light transparency and efficient photon transport [15]. This limitation can be attributed to several factors, including particle size, morphology, surface area, and the synthesis method employed. Therefore, enhancing the photocatalytic activity of CdS nanoparticles remains a crucial area of research [16], particularly in the context of semiconductor-based photocatalysis, where efficient light absorption and charge carrier separation are essential for driving redox reactions under solar irradiation [17]. The activity of CdS is highly dependent on the generation, separation, and utilization of electrons and holes produced upon light absorption. Enhancing these aspects can lead to improved photocatalytic performance [18–20]. CdS nanoparticles exhibit unique physical properties that make them particularly interesting for photocatalytic applications [21–25]. The physical properties of CdS nanoparticles can vary depending on their size, shape, and the synthesis method used [4, 25, 26].

The hydrothermal method offers several advantages for the preparation of nanoparticle materials, including low-temperature processing and avoidance of organometallic or toxic precursors [25, 27].

The optical and electronic properties of CdS can be tuned by controlling the size and shape of the nanoparticles [28–30]. Studies have demonstrated that the photocatalytic hydrogen evolution activity of cd_1s_{1-x} is strongly influenced by its morphology, crystal structure, crystallinity, and particle size. For instance, quantum dots may have different properties compared to bulk materials. The band gap of cd_1s_{1-x} was found to be approximately 2.37 eV, which corresponds to an absorption edge of approximately 525 nm in the visible light region. Moreover, cd_1s_{1-x} nanoparticles can exist in different crystalline forms, and this has a significant impact on their electronic, catalytic, and optical properties [9, 31–34].

In the present study, we report a simple and cost-effective hydrothermal synthesis route for cd_1s_{1-x} nanoparticles, which exhibit high photocatalytic activity for the degradation of organic pollutants under visible light irradiation at relatively low temperatures.

The optical properties and photocatalytic activity of as-synthesized cd_1s_{1-x} nanoparticles were systematically studied. The underlying mechanism responsible for the enhanced photocatalytic performance was explored and discussed. We believe that this study may pave the way for further enhancement of the photocatalytic properties of cd_1s_{1-x} and offers promising potential for the future large-scale application of In-doped cd_1s_{1-x} nanostructures based on this simple preparation method.

2. EXPERIMENTAL

2.1. Preparation of CD_1S_{1-x} nanoparticle.

cd_1s_{1-x} nanoparticles were synthesized via a facile hydrothermal method using cadmium acetate ($Cd(CH_3COO)_2{\cdot}2H_2O$) as the cadmium source and thiourea ($(NH_2)_2CS$) as the sulfur source. The concentration of cadmium acetate was fixed at 0.0076 mol/g, and the thiourea concentration was systematically varied (0.0026 mol/g) to investigate the influence of the sulfur ion content on the photocatalytic properties of the resulting cd_1s_{1-x} nanoparticles. The precursors were separately dissolved in an ethanol–water mixture (total volume: 80 mL) in a 1:1 volume ratio (V_ethanol*: V_water). The mixture was transferred to the inner tube of an autoclave, sealed, and maintained at 120℃ for 10 h. After the hydrothermal reaction was complete, the autoclave was allowed to cool naturally to room temperature. The resulting yellow precipitate was collected by centrifugation, washed three times alternately with absolute ethanol and deionized water to eliminate any residual ions or impurities, and subsequently dried in an oven at 60℃ for 3 hours and annealed at 400℃ for 2h. For comparison, additional samples were prepared by varying the thiourea concentration to 0.0026, 0.0039, and 0.0053 mol/g, corresponding to samples A, B, and C, respectively. The detailed precursor ratios are summarized in Table (1).

2.2. Characterization Techniques of CD_1S_{1-x} nanoparticle.

The crystalline structures of the as-prepared cd_1s_{1-x} samples were analyzed using powder X-ray diffraction (XRD) on a Y-2000 automated diffractometer (D/max, 30 kV) equipped with Cu Kα radiation (λ = 0.154178 nm). The data were collected at a scanning rate of 0.04° 2θ s^{-1} over the appropriate diffraction angle range.

The surface morphology and microstructure of the samples were examined using field-emission scanning electron microscopy (FE-SEM; JEOL JSM-6700F).

The optical properties were investigated using UV–vis diffuse reflectance spectroscopy (UV–vis DRS) recorded with a PerkinElmer Lambda 350 spectrophotometer over the wavelength range of 200–800 nm.

3. RESULTS AND DISCUSSION

3.1. Crystal structures of CD_1S_{1-x} samples.

Figure (1)(a–c) shows the X-ray diffraction (XRD) patterns of the cd_1s_{1-x} samples A, B, and C. All samples were maintained at 120 ℃ for 12 h during the hydrothermal process and subsequently annealed at 400 ℃ to improve crystallinity and remove residual organic species [27, 35, 36]. The diffraction peaks for all samples match

Table[1]: show the different degradation efficiency of cd_1s_{1-x} nanoparticle

Sample	X in cd_1s_{1-x}	Cd:S Molar Ratio [mol/g]			Band gap (eV)	Time for Full Degradation (min)	Degradation Efficiency (%)	Rate Constant k (min^{-1})
		Cd (mol/g)	S (mol/g)	S/Cd Ratio				
A	0.6579	0.0076	0.0026	0.3421	2.76	70	92%	0.012
B	0.4868	0.0076	0.0039	0.5132	2.70	70	94%	0.019
C	0.3026	0.0076	0.0053	0.6974	2.37	70	100%	0.021

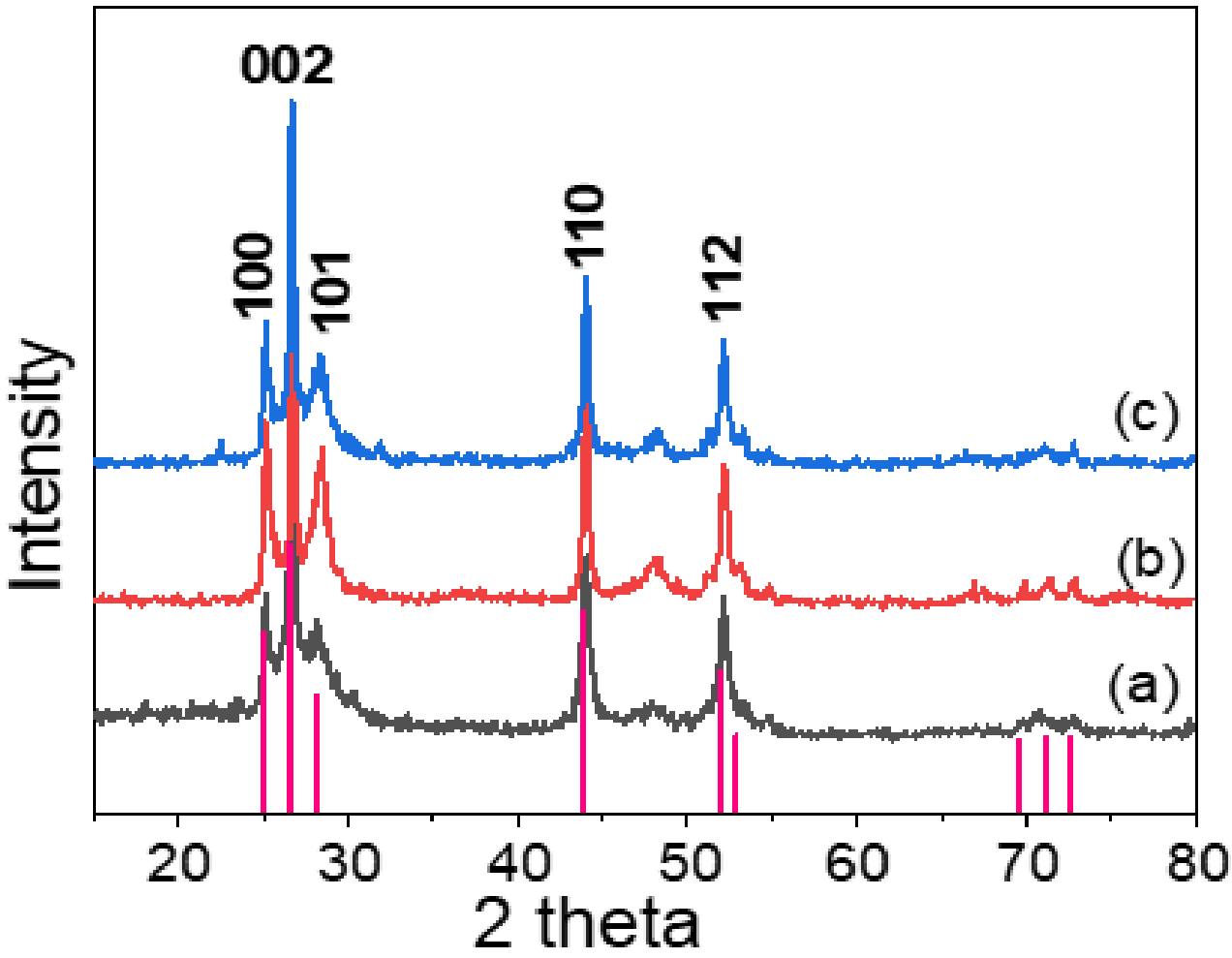

Figure 1. displays the X-ray diffraction (XRD) patterns of cd_1s_{1-x} samples synthesized with the mole ratio x of 0.6579 (A), 0.4868 (B), and 0.3026 (C), respectively

well with the monoclinic -Greenockite phase of CdS (JCPDS No. 02-0549). The characteristic reflections appearing at $2\theta \approx 24.95°$, 26.60°, 28.24°, and 51.95° correspond to the (100), (002), (101), (110), and (112) crystal planes, respectively, confirming the formation of phase-pure CdS.

The sharp and well-defined peaks suggest that the synthesized samples possessed good crystallinity. The highest peak, corresponding to the (002) plane, remained nearly constant across all samples; this is expected given that the samples were synthesized under identical conditions, indicating the successful formation of crystalline cd_1s_{1-x}. As the S^{2-} concentration increased, noticeable changes in the intensity and sharpness of the diffraction peaks were observed [5, 30]. The dominant (002) reflection is a characteristic feature of the hexagonal α-greenockite CdS structure and indicates a preferred orientation of crystallites along the c-axis. The nearly unchanged 2 position of this peak across all cd_1s_{1-x} samples confirms that varying the sulfur content does not alter the fundamental lattice parameters, indicating that the introduced sulfur vacancies are too small in concentration to produce measurable lattice distortion. However, the increased peak intensity with higher sulfur content reflects improved crystallinity and the formation of smaller, more well-defined CdS nanoparticles.

This suggests that the crystallinity of cd_1s_{1-x} improved at higher sulfur contents [37, 38]. A characteristic peak corresponding to pure sulfur was observed in sample C, which is associated with x=0.3026 (Figure (1)(c)). Using the Scherrer equation (1), the average crystallite size was calculated and found to vary marginally with changes in

the Cd:S molar ratio [30].

$$D = 0.9\lambda/\beta cos\theta \quad (1)$$

where D is the crystal size, λ is the wavelength of the X-ray, β is the full width at half maximum (FWHM), and is Bragg's angle. The crystal sizes of cd_1s_{1-x} calculated from the (002) peak of the sample were 4.56, 5.17, 4.43, 5.96, 3.6, and 3.6 nm, respectively. The enhancement in crystallinity and decrease in particle size with increasing sulfur concentration may be attributed to the more complete reaction between Cd^{2+} and S^{2-} ions during the hydrothermal process, resulting in better crystal formation [25, 39–41]. The introduction of a large amount of $SC(NH_2)_2$ into cd_1s_{1-x} may have introduced impurities into the structure, which may contribute to a reduction in photocatalytic activity. No significant changes were observed in the crystalline structure of the cd_1s_{1-x} peaks because of the minimal presence of $SC(NH_2)_2$.

XPS.

Figure (2)(a and b) shows the high-resolution XPS spectra of the S 2p and Cd 3d core levels for the CdS sample prepared with a Cd:S ratio of 7.6:5.3 (sample C). To compensate for surface charging effects, all binding energies were calibrated using the C 1s peak at 284.66 eV [2, 42]. The Cd 3d spectrum (Figure (2)b) exhibits two well-defined peaks at binding energies of 404.915 and 411.7 eV, corresponding to the Cd $3d^{5/2}$ and Cd $3d^{3/2}$ states, respectively. These peaks arise from the spin–orbit splitting of the Cd 3d core level and are characteristic of Cd^{2+} in the CdS lattice. The high-resolution S 2p spectrum displays two distinct peaks at 161.1 and 162.2 eV, assigned to the S $2p^{3/2}$ and S $2p^{1/2}$ components, respectively. The low-resolution S 2s spectrum displays two distinct peaks at 161.1 and 162.2 eV, assigned to the S $2p^{3/2}$ and S $2p^{1/2}$ components, respectively. These binding energies are typical of s^{2-} ions bonded to Cd^{2+}, confirming the formation of Cd–S bonds. Slight peak broadening and minor binding energy shifts in the S 2p region suggest charge redistribution around sulfur atoms, which may be associated with lattice defects, such as sulfur vacancies or local non-stoichiometry. The peak at approximately 226.5 eV binding energy is primarily attributed to the sulfur 2s (S 2s) core level. A weak O 1s signal, typically observed in the binding energy range of 531–533 eV, is commonly detected in CdS XPS spectra. This oxygen signal does not indicate bulk oxygen incorporation into the CdS lattice but is attributed to surface-adsorbed oxygen species, hydroxyl groups, or adsorbed water molecules. The XPS results are in good agreement with the XRD analysis, confirming that sulfur is successfully incorporated into the Cd lattice without the formation of a separate crystalline sulfur phase at low sulfur concentrations (Cd:S = 8:0.8). At higher sulfur ratios, additional sulfur-related diffraction peaks are expected owing to phase separation or excess sulfur. The absence of undesired oxide phases and the presence of defect-related chemical environments are highly beneficial. These defects can act as charge trapping centers, suppressing electron–hole recombination, enhancing charge carrier separation, and promoting interfacial redox reactions. Collectively, these features contribute to the enhanced photocatalytic performance of CdS nanoparticles.

3.2. Morphology of the synthesized cd_1s_{1-x} nanoparticles.

The morphology and nanostructure of the synthesized cd_1s_{1-x} were characterized using SEM. The SEM image of Sample (A), prepared with X= 0.6579, reveals the presence of large particles with an approximate diameter of 4 μm. This particle size is significant, supporting the idea that cd_1s_{1-x} synthesized with a smaller $SC(NH_2)_2$ ratio primarily forms bulk-like structures under these synthesis conditions, as shown in Figure (3)(A). To investigate the mechanism behind the increasing $SC(NH_2)_2$ concentration in the preparation of cd_1s_{1-x} nanoparticles, samples prepared at different stages of synthesis were systematically analyzed to investigate the formation process, as presented in Figures (3)(A-C). The SEM image of Sample B, shown in Figure (3)(B), reveals uniformly distributed spherical particles with diameters ranging from approximately 300 nm to 100 nm. However, these particles tended to aggregate, forming larger microspheres with diameters of approximately 2μm. Figure (3)(C) displays the SEM image of sample C, synthesized with x=0.3026, highlighting the crystalline nature of the resulting structures. Most of the spheres appeared to be aggregated with smaller particles, and the aggregated spheres exhibited good morphology, with a diameter range of 100–150 nm. The surface morphology of the crystalline cd_1s_{1-x} sample with x=0.3026, as revealed by SEM, is presented in Figure (3)(c). It appears that the concentration of s^{2-} plays a significant role, as increasing the s^{2-} concentration leads to a gradual decrease in particle size. Additionally, the impact of s^{2-} addition on particle size during cd_1s_{1-x} synthesis is noteworthy. Thiourea acts as a sulfur source in the synthesis of cd_1s_{1-x}. When heated, especially in hydrothermal processes, it gradually decomposes to release sulfide ions (s^{2-}) [43, 44]. These ions react with Cd^{2+} to form cd_1s_{1-x} nanoparticles. Low $SC(NH_2)_2$ concentration, slower sulfur release, fewer nucleation sites, and formation of larger, bulk-like particles [45]. Increasing the concentration of $SC(NH_2)_2$ enhances the sulfur release rate, which accelerates nucleation and yields a larger population of smaller nanoparticles. The reduced particle size increases the density of exposed active surface

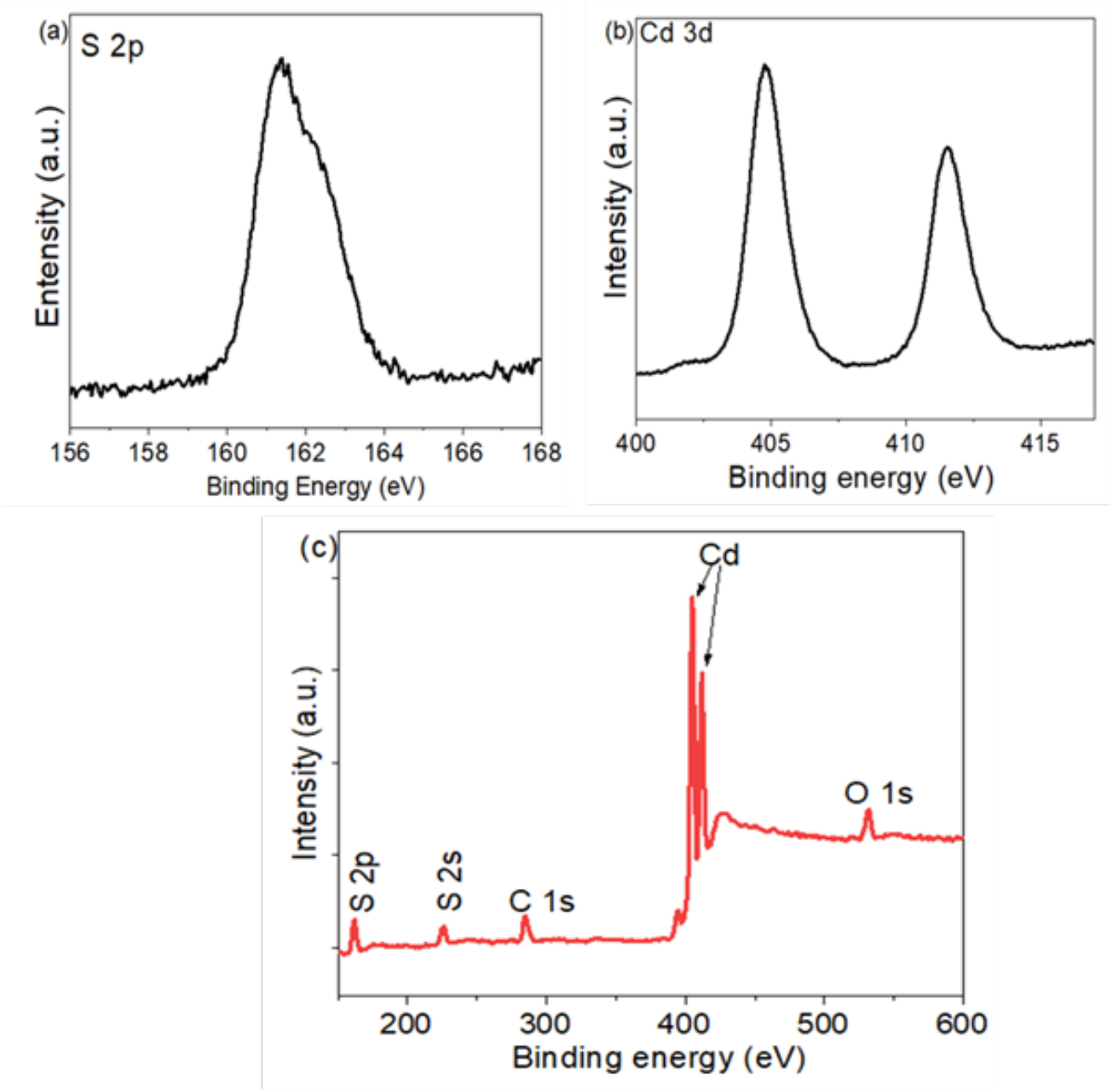

Figure 2. High and low resolution XPS spectra for cd_1s_{1-x} Nanoparticles (a) S 2p, (b) Cd 3d, and low resolution (c) sample C.

sites and shortens charge-carrier diffusion paths, thereby suppressing recombination. Additionally, the transition from aggregated microspheres to dispersed nanoparticles produces a more homogeneous suspension and improves contact with Rh-B molecules. Collectively, these morphological and charge-transfer advantages account for the enhanced photocatalytic degradation efficiency toward Rh-B.

3.3. Optical Properties of cd_1s_{1-x}

UV-vis absorption spectroscopy was employed to investigate the optical properties of the synthesized cd_1s_{1-x} nanoparticles. As illustrated in Figure (4), cd_1s_{1-x} nanoparticles exhibited strong absorption in the visible region, which is characteristic of cd_1s_{1-x} semiconductors. The enhanced visible-light absorption observed in smaller particles, especially in sample C, can be attributed to their good crystallinity. This crystallinity reduces defect-related trap states, which typically widen the band gap. Additionally, the formation of smaller nanoparticles induces partial quantum confinement effects, thereby subtly altering electronic transitions. These combined factors enable more efficient utilization of solar light and significantly enhance photocatalytic activity.

The observation of cd_1s_{1-x} samples revealed that the absorption edge for most nanoparticles occurred at approximately 440 nm, which corresponds to a specific band gap energy. However, sample C showed an unusual absorption edge at 525 nm, suggesting that it may have different structural or electronic properties com-

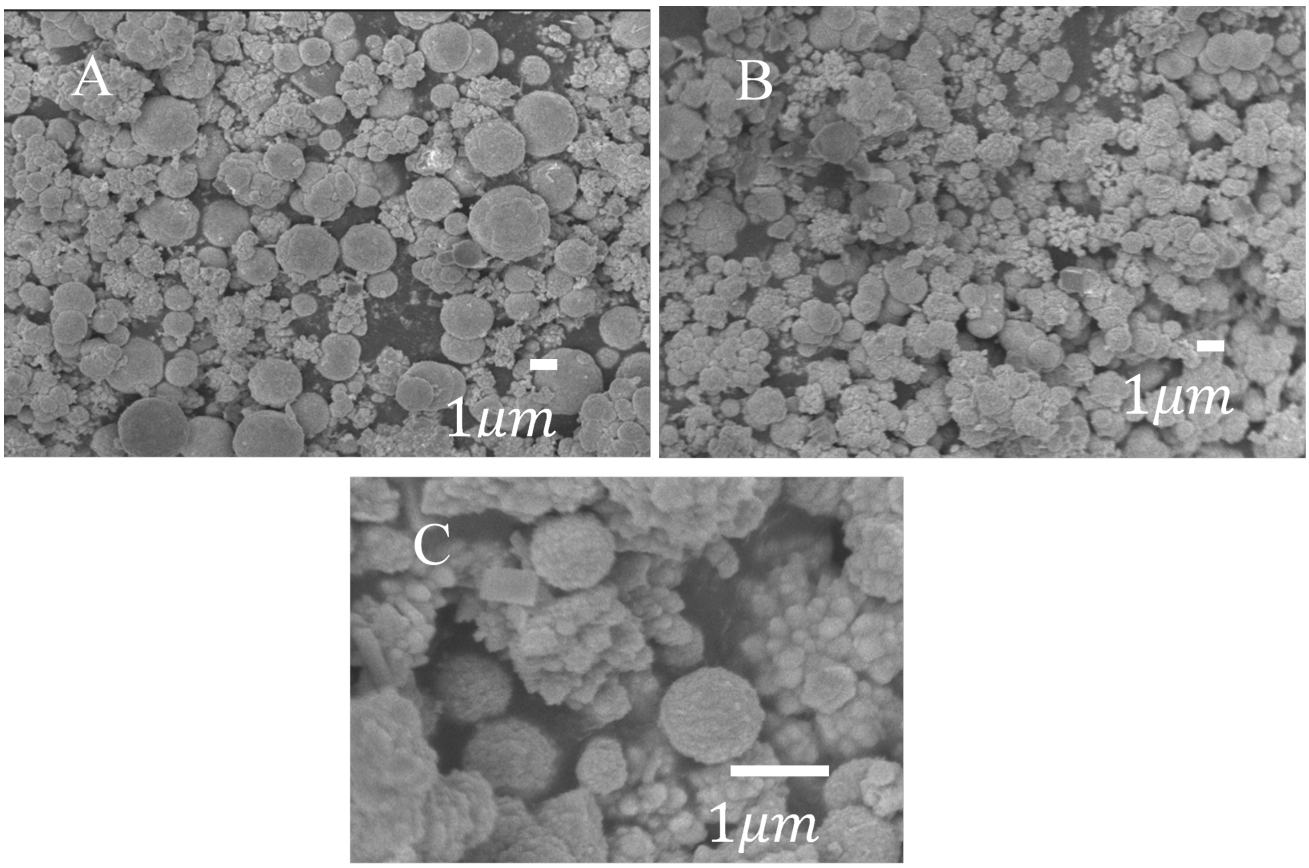

Figure 3. SEM images of alpha-Greenokite cd_1s_{1-x} samples synthesized with the mole ratio x of 0.6579 (A), 0.4868 (B), and 0.3026 (C), respectively

pared to the other samples. The calculated band gap values were 2.76, 2.70, and 2.37 eV for samples A, B, and C, respectively.

In this study, enhanced absorption of simulated solar light was observed with increasing concentrations of s^{2-} in the synthesis process. Increasing the s^{2-} ratio results in enhanced peak intensity, improved crystallinity, decreased band gap, and decreased particle size, collectively leading to improved photocatalytic activity. This also causes a red shift in the absorption edge of the cd_1s_{1-x} crystals toward the visible region. This red shift, along with improvements in morphology and crystallinity, confirms that controlling the sulfur ratio is a viable strategy for optimizing cd_1s_{1-x} photocatalysts. The gradual decomposition of the precursor releases sulfide ions (s^{2-}), which react with Cd^{2+} to form cd_1s_{1-x} nanoparticles [29–31].

Our observation that increasing the sulfur ratio shifts the absorption edge toward longer wavelengths and enhances visible-light absorption agrees with recent reports, wherein sulfur source variations or sulfur-vacancy engineering resulted in similar band-gap tuning and visible-light harvesting in cd_1s_{1-x} [16]. The optical absorption near the band edge of a crystalline semiconductor is commonly described by the following equation [46, 47]:

$$E = 1242/\lambda \tag{2}$$

3.4. Photocatalytic Activity.

To evaluate the photocatalytic activity, the degradation of Rh B under simulated solar light was used as a model reaction. Figure (5) shows the photodegradation efficiency of Rh-B for cd_1s_{1-x} samples synthesized with varying S/Cd ratios, as shown in Table (1). The degradation process was monitored by measuring the decrease in absorbance at 553 nm, the characteristic peak of Rh-B. The results indicate that the photocatalytic activity is significantly influenced by the ratio. The photocatalytic performance varied noticeably with the S/Cd ratio.

At 55 min, Sample A (0.3421 S/Cd) exhibited a relatively low degradation efficiency (75%), whereas Sample B (0.5132 S/Cd) reached 90% degradation. Sample C (0.6974 S/Cd) showed comparable activity at this stage, attaining 90% degradation. After 70 min, the differences became more pronounced. Sample A achieved 92% degradation, while Sample B reached 94%. Notably, Sample C demonstrated the highest photocatalytic activity, achieving complete (100%) degradation within the same time.

This corresponds to the highest degradation efficiency

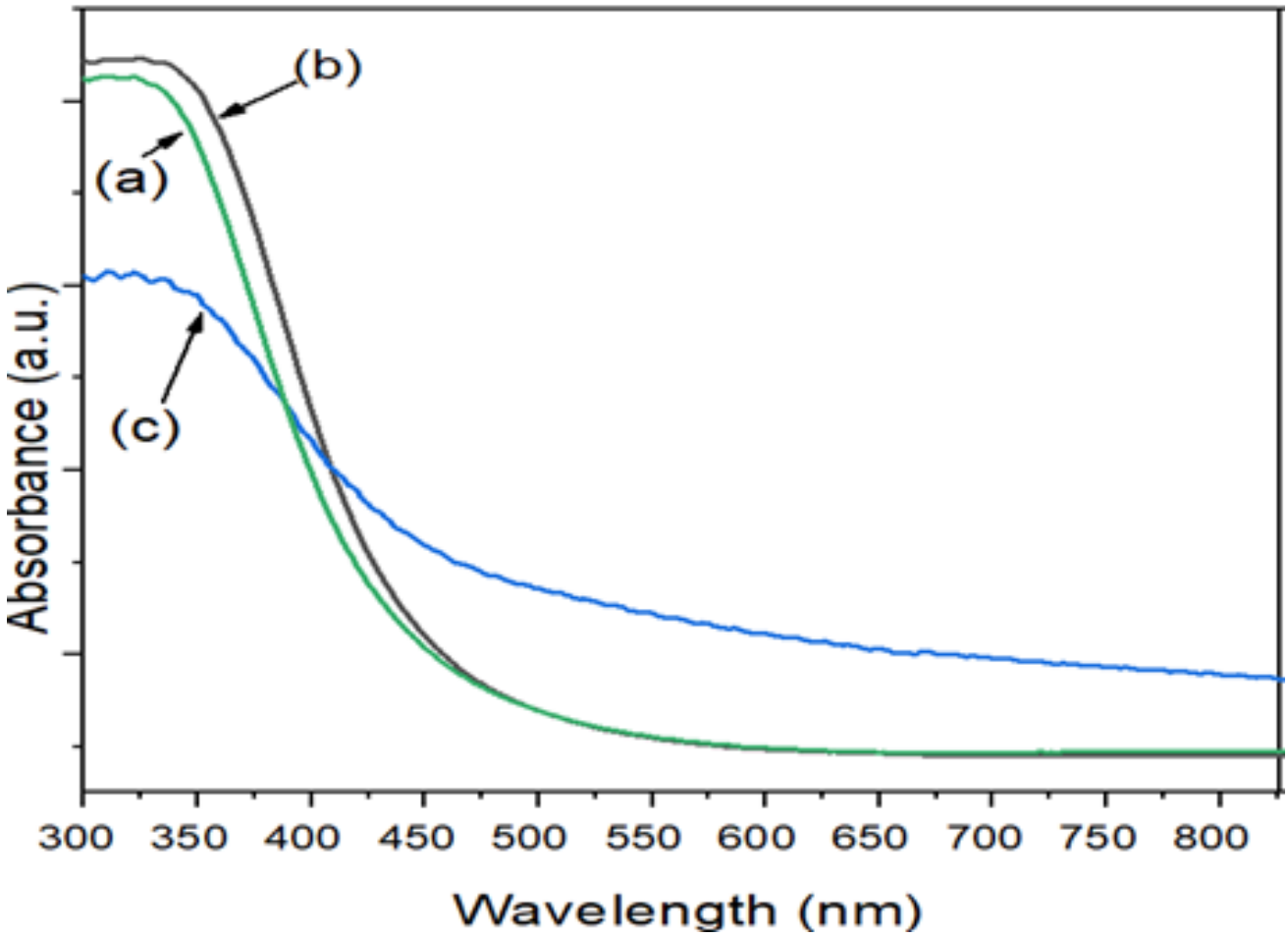

Figure 4. UV–Vis absorption of cd_1s_{1-x} samples synthesized with the mole ratio x of 0.6579 (A), 0.4868 (B) and 0.3026 (C), respectively

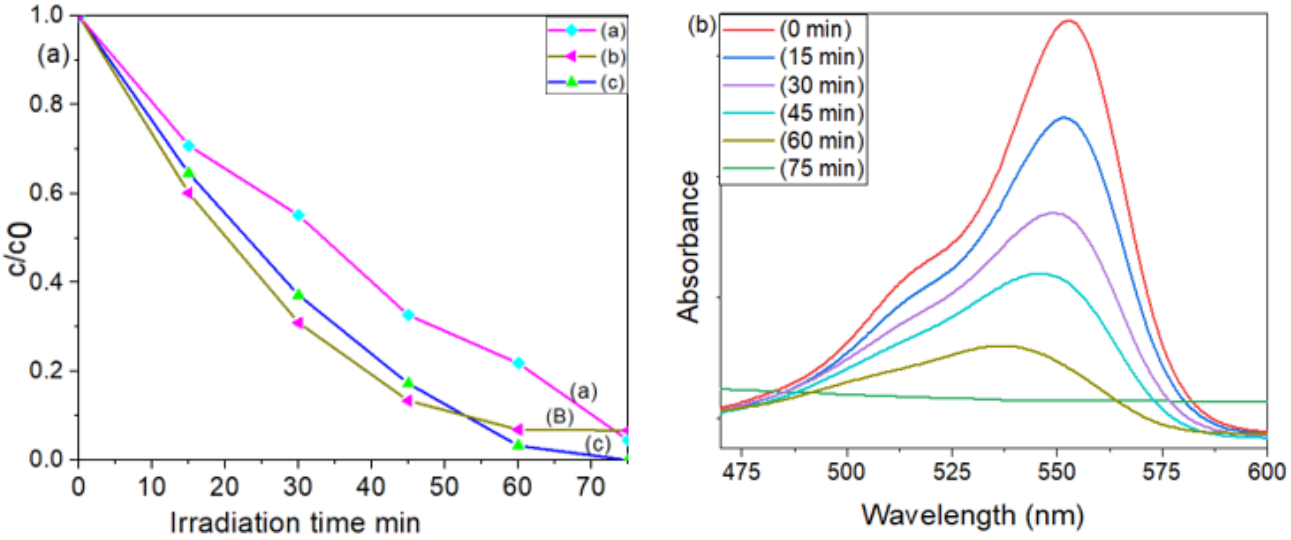

Figure 5. shows (a) the photodegradation efficiency of Rhodamine B (Rh-B) for cd_1s_{1-x} samples with x = 0.6579 (A), 0.4868 (B), and 0.3026 (C), and (b) the absorbance spectra of Rh-B for sample C.

achieved among the tested samples, as shown in Table (1).

UV–Vis measurements reveal a progressive red-shift of the absorption edge and a decrease in the optical band gap from 2.76 eV (sample A) to 2.37 eV (sample C) as the thiourea (S) ratio increases. This behavior is consistent with recent reports, wherein variations in the sulfur source or deliberate introduction of sulfur vacancies resulted in similar band-gap tuning and extended visible-light absorption [38]. The red-shift in our samples is

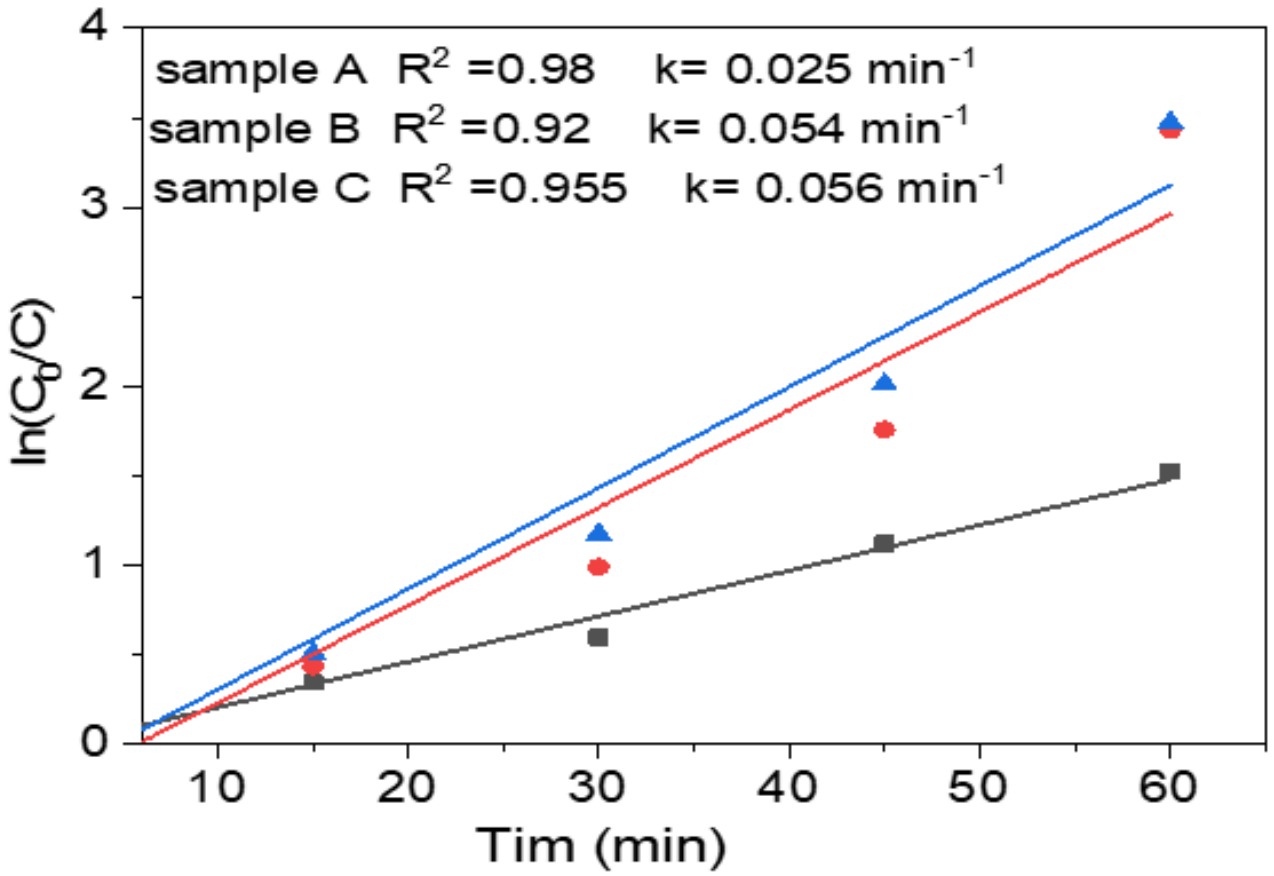

Figure 6. Linear plot of ln(C_0/C) versus irradiation time showing the pseudo-first-order kinetic behavior of RhB dye degradation over the cd_1s_{1-x} photocatalyst under visible-light irradiation

accompanied by a morphology change from aggregated microspheres to dispersed nanoparticles (SEM, Figure 3), which increases the surface area and active-site accessibility. Thus, band-gap narrowing and enhanced surface exposure explain the observed improvement in Rh-B photodegradation rates for sulfur-rich samples. These trends are in agreement with the literature, which links sulfur-deficiency/defect engineering and precursor-ratio control to improved visible-light harvesting and photocatalytic activity.

The photocatalytic efficiency obtained in this study is comparable to, and in some cases higher than, values reported for cd_1s_{1-x} synthesized using more complex procedures. This improvement is attributed to improved crystallinity, reduced particle size, and better light absorption.

The photocatalytic performance of the cd_1s_{1-x} samples was further evaluated by analyzing the degradation kinetics of RhB under visible-light irradiation. The degradation behavior generally follows the Langmuir–Hinshelwood (L–H) model, which simplifies to a pseudo-first-order kinetic expression at low dye concentrations. The corresponding rate equation is as follows:

$$ln(C_0/C) = k_1 t \quad (3)$$

where k_1 (min^{-1}) is the apparent pseudo-first-order rate constant.

Figure (5) shows the plots of ln(C_0/C) versus irradiation time for samples A, B, and C. All samples exhibited a strong linear relationship ($R^2 \approx 0.89$–0.95), confirming that the degradation of RhB proceeded via pseudo-first-order kinetics. The rate constants (k_1) were found to be 0.025 min^{-1}, 0.054 min^{-1} and 0.056 min^{-1} for samples A, B, and D, respectively. These results clearly demonstrate that the photocatalytic degradation rate increased with increasing sulfur content. Sample C exhibited the highest rate constant, more than double that of sample A, indicating significantly improved photocatalytic activity.

3.5. Mechanism of photocatalytic activity

Increasing the S^{2-} concentration enhances the peak intensity and sharpness, indicating higher crystallinity. Improved crystallinity reduces defect recombination centers, thereby enhancing photogenerated charge separation.

Figure (5) clearly demonstrates that pure cd_1s_{1-x} can degrade Rh-B under simulated solar light irradiation. As revealed by the XRD patterns, increasing the S_{2-} concentration enhances the peak intensity and sharpness, resulting in higher crystallinity. Moreover, improved crystallinity reduces the number of defect recombination cen-

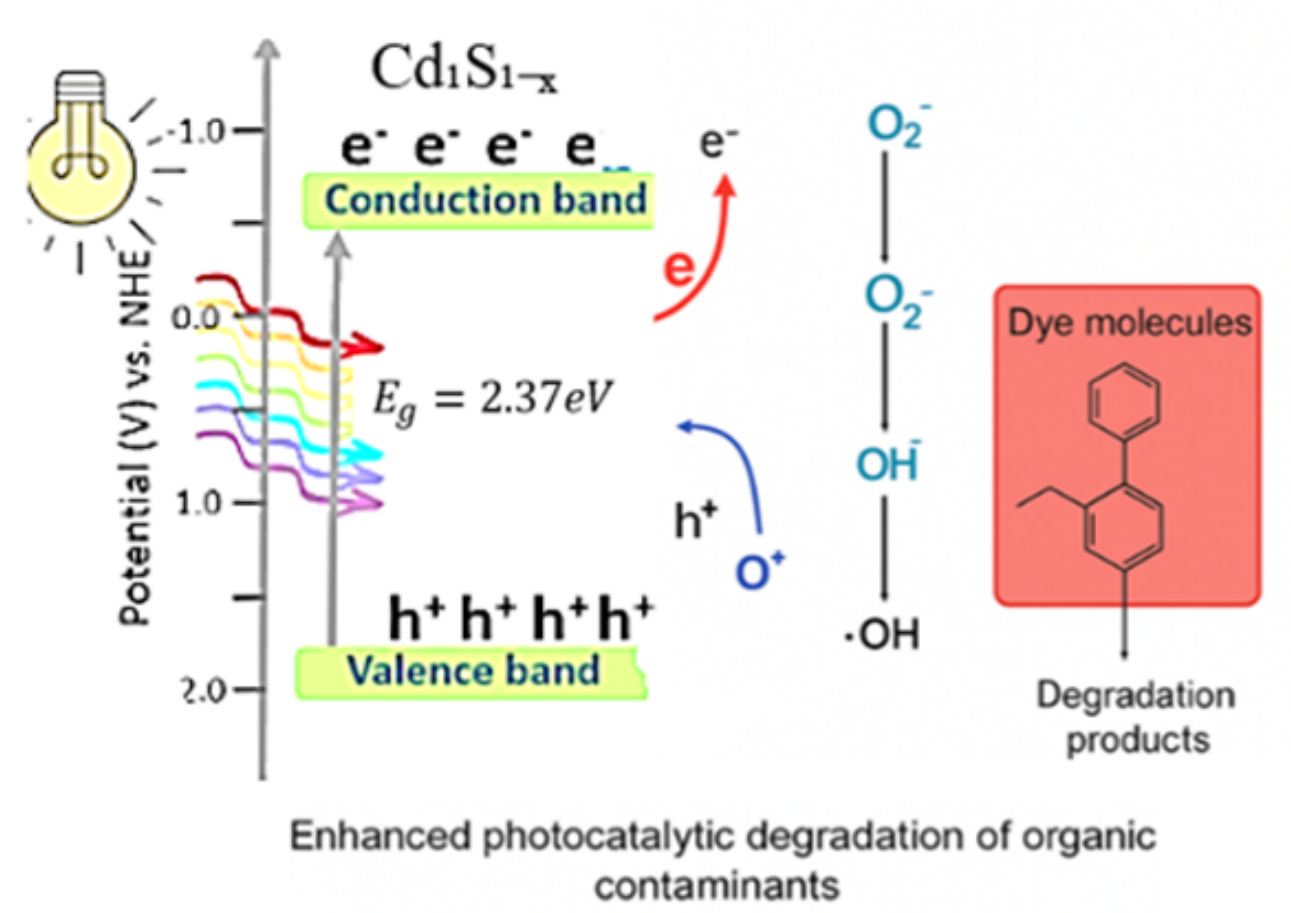

Figure 7. Schematic illustration of the cd_1s_{1-x} nanoparticles photocatalytic degradation mechanism of RhB under visible-light irradiation.

ters and enhances photogenerated charge separation. The UV-Vis absorption spectra indicate that the cd_1s_{1-x} nanoparticle possesses a slightly narrower band gap than that of a cd_1s_{1-x} microparticle. Samples prepared with higher sulfur content exhibited well-defined nanoparticles instead of aggregated microspheres. Nanoparticles offer an increased surface area and reactive sites, which contribute to a higher photocatalytic rate. Additionally, band gap modulation enhances the alignment of the cd_1s_{1-x} nanoparticle's electronic structure with the solar spectrum, thereby facilitating more efficient light absorption. Consequently, the improved spatial separation of photogenerated electron–hole pairs contributes to enhanced photocatalytic performance in the degradation of organic contaminants. This structural feature allows photogenerated electron–hole (e^-/h^+) pairs to migrate more efficiently to the surface, where they can interact with redox species in the surrounding solution [10, 19]. This reduces the likelihood of charge carrier recombination and enhances the generation of reactive species responsible for the degradation of organic pollutants [19, 26]. Therefore, cd_1s_{1-x} a promising visible-light-driven photocatalyst, although its stability and photo-corrosion remain challenges that are often addressed through compositing or surface modification. Upon excitation, the photogenerated electrons (e^-) and holes (h^+) function as potent reducing and oxidizing agents, respectively, driving redox reactions on the catalyst surface [1, 9]. Photogenerated electrons reduce dissolved O_2 to form superoxide radicals ($\bullet O_2^-$), while holes oxidize H_2O or OH^- to generate hydroxyl radicals (•OH), both of which are key to the degradation of dye molecules into harmless compounds (Figure 6) [10, 27]:

$$e^- + O_2 \rightarrow \cdot O_2^-$$

$$h^+ + H_2O \rightarrow \cdot OH + H^+$$

$$h^+ + OH^- \rightarrow \cdot OH$$

This synergistic effect of charge carrier separation and radical generation makes Cd S S1-x an efficient photocatalyst for environmental remediation applications (Figure 7).

4. CONCLUSION

In this study, cd_1s_{1-x} nanoparticles were successfully synthesized via a simple hydrothermal method using various Cd:S molar ratios to investigate the effect of sulfur concentration on photocatalytic activity. Struc-

tural, morphological, and optical characterizations using X-ray diffraction (XRD), scanning electron microscopy (SEM), and UV–vis spectroscopy confirmed the formation of crystalline cd_1s_{1-x} with visible light absorption and tunable properties influenced by the precursor concentration. Among the nanoparticles, the one with the highest photocatalytic degradation efficiency under visible light achieved nearly complete degradation within 73 min. This enhanced performance is attributed to improved crystallinity, optimized particle size distribution, higher surface area, and more effective separation of photogenerated electron–hole pairs. This study demonstrates that the sulfur/cadmium (S/Cd) ratio plays a crucial role in tailoring the structural and photocatalytic properties of cd_1s_{1-x} nanoparticles. The optimal S/Cd ratio of 0.697 offers a promising approach for developing efficient visible-light-driven photocatalysts for environmental remediation applications. This work elucidates the fundamental photophysical processes underlying the photocatalytic activity of cd_1s_{1-x}, aiming to advance the development and optimization of solar energy conversion technologies.

REFERENCES

[1] X. Xue et al., "Piezo-potential enhanced photocatalytic degradation of organic dye using zno nanowires," *Nano Energy*, vol. 13, pp. 414–422, 2015.

[2] M. Naushad, T. Ahamad, B. M. Al-Maswari, A. A. Alqadami, and S. M. Alshehri, "Nickel ferrite bearing nitrogen-doped mesoporous carbon as efficient adsorbent for the removal of highly toxic metal ion from aqueous medium," *Chem. Eng. J.*, vol. 330, pp. 1351–1360, 2017.

[3] B. M. Al-Maswari et al., "Synthesis and characterization of a nanocomposite electrode of titanium ferrite n-doped carbon for high-performance supercapacitor applications," *Inorg. Chem. Commun.*, p. 114 890, 2025.

[4] S. Sharma, V. Dutta, P. Raizada, A. Hosseini-Bandegharaei, P. Singh, and V.-H. Nguyen, "Tailoring cadmium sulfide-based photocatalytic nanomaterials for water decontamination: A review," *Environ. Chem. Lett.*, vol. 19, no. 1, pp. 271–306, 2021.

[5] J. Zhang et al., "Energy environ. sci.," *Energy & Environ. Sci.*, vol. 4, p. 675, 2011.

[6] Y. M. Jamil, H. M. Al-Maydama, A. N. Al-Hakimi, G. Y. Al-Mahwiti, H. M. Ibrahim, and B. Al-Akhali, "The characterization, antibacterial and antioxidant of phytosynthesized zinc oxide nanoparticles using aloe fleurentinorum leaves extract," *Sana'a Univ. J. Appl. Sci. Technol.*, vol. 2, no. 4, pp. 339–347, 2024.

[7] Y.-J. Yuan, D. Chen, Z.-T. Yu, and Z.-G. Zou, "Cadmium sulfide-based nanomaterials for photocatalytic hydrogen production," *J. Mater. Chem. A*, vol. 6, no. 25, pp. 11 606–11 630, 2018.

[8] U. Abdullah, M. Ali, and E. Pervaiz, "An inclusive review on recent advancements of cadmium sulfide nanostructures and its hybrids for photocatalytic and electrocatalytic applications," *Mol. Catal.*, vol. 508, p. 111 575, 2021.

[9] A. A. A. AL-Adhreai, A. Abdulwahab, and A. Al-Hammadi, "Structural, optical and cytotoxic analysis of sr-doped cus nanoparticles for lung cancer applications," *Sana'a Univ. J. Appl. Sci. Technol.*, vol. 3, no. 4, pp. 990–998, 2025.

[10] A. Abdulkarem, E. Elssfah, N.-N. Yan, G. Demissie, and Y. Yu, "Photocatalytic activity enhancement of cds through in doping by simple hydrothermal method," *J. Phys. Chem. Solids*, vol. 74, no. 4, pp. 647–652, 2013.

[11] A. Meng, B. Zhu, B. Zhong, L. Zhang, and B. Cheng, "Direct z-scheme tio2/cds hierarchical photocatalyst for enhanced photocatalytic h2-production activity," *Appl. Surf. Sci.*, vol. 422, pp. 518–527, 2017.

[12] S. M. Al-Jawad, S. N. Rafic, and M. M. Muhsen, "Preparation and characterization of polyaniline–cadmium sulfide nanocomposite for gas sensor application," *Mod. Phys. Lett. B*, vol. 31, no. 26, p. 1 750 234, 2017.

[13] N. Memarian, S. M. Rozati, I. Concina, and A. Vomiero, "Deposition of nanostructured cds thin films by thermal evaporation method: Effect of substrate temperature," *Materials*, vol. 10, no. 7, p. 773, 2017.

[14] B. Fabbri, A. Gaiardo, V. Guidi, C. Malagù, and A. Giberti, "Photo-activation of cadmium sulfide films for gas sensing," *Procedia Eng.*, vol. 87, pp. 140–143, 2014.

[15] K. Yang et al., "Recent advances in cds-based photocatalysts for co2 photocatalytic conversion," *Chem. Eng. J.*, vol. 418, p. 129 344, 2021.

[16] Q. Zhu et al., "Effect of the organic sulfur source on the photocatalytic activity of cds," *RSC Adv.*, vol. 12, no. 18, pp. 11 262–11 271, 2022.

[17] J. P. Molina-Jiménez, S. D. Horta-Piñeres, S. Castillo, J. Izquierdo, and D. Avila, "Ultra-thin films of cds doped with silver: Synthesis and modification of optical, structural, and morphological properties by the doping concentration effect," *Coatings*, vol. 15, no. 4, p. 431, 2025.

[18] J.-Y. Li, Y.-H. Li, M.-Y. Qi, Q. Lin, Z.-R. Tang, and Y.-J. Xu, "Selective organic transformations over cadmium sulfide-based photocatalysts," *ACS Catal.*, vol. 10, no. 11, pp. 6262–6280, 2020.

[19] Z. Gao, N. Liu, D. Wu, W. Tao, F. Xu, and K. Jiang, "Graphene–cds composite, synthesis and enhanced photocatalytic activity," *Appl. Surf. Sci.*, vol. 258, no. 7, pp. 2473–2478, 2012.

[20] J. Zhao, H. Yang, Y. Li, and K. Lu, "Photocatalytic activity of cds nanoparticles enhanced by the interaction between piezotronic effect and phase junction," *J. Alloy. Compd.*, vol. 815, p. 152 494, 2020.

[21] J. Yu, Y. Yu, P. Zhou, W. Xiao, and B. Cheng, "Morphology-dependent photocatalytic h2-production activity of cds," *Appl. Catal. B: Environ.*, vol. 156, pp. 184–191, 2014.

[22] H. Meng et al., "Synthesis and photocatalytic activity of tio2@cds and cds@tio2 double-shelled hollow spheres," *J. Alloy. Compd.*, vol. 527, pp. 30–35, 2012.

[23] Y. Yu, Y. Huang, Y. Yu, Y. Shi, and B. Zhang, "Design of continuous built-in band bending in self-supported cds nanorod-based hierarchical architecture for efficient photoelectrochemical hydrogen production," *Nano Energy*, vol. 43, pp. 236–243, 2018.

[24] X. Xu et al., "Controlled growth from zns nanoparticles to zns–cds nanoparticle hybrids with enhanced photoactivity," *Adv. Funct. Mater.*, vol. 25, no. 3, pp. 445–454, 2015.

[25] N. Loudhaief, H. Labiadh, E. Hannachi, M. Zouaoui, and M. B. Salem, "Synthesis of cds nanoparticles by hydrothermal method and their effects on the electrical properties of bi-based superconductors," *J. Supercond. Nov. Magn.*, vol. 31, no. 8, pp. 2305–2312, 2018.

[26] H. K. Judran, N. A. Yousif, and S. M. Al-Jawad, "Preparation and characterization of cds prepared by hydrothermal method," *J. Sol-Gel Sci. Technol.*, vol. 97, no. 1, pp. 48–62, 2021.

[27] L. Zhang, Z. Cheng, D. Wang, and J. Li, "Preparation of popcorn-shaped cds nanoparticles by hydrothermal method and their potent photocatalytic degradation efficiency," *Mater. Lett.*, vol. 158, pp. 439–441, 2015.

[28] J. Zhang, S. Wageh, A. Al-Ghamdi, and J. Yu, "New understanding on the different photocatalytic activity of wurtzite and zinc-blende cds," *Appl. Catal. B: Environ.*, vol. 192, pp. 101–107, 2016.

[29] T. Serrano, I. Gómez, R. Colás, and J. Cavazos, "Synthesis of cds nanocrystals stabilized with sodium citrate," *Colloids Surfaces A: Physicochem. Eng. Aspects*, vol. 338, no. 1–3, pp. 20–24, 2009.

[30] B. Vaishnavi, T. Sreelakshmi, M. Rahina, M. Murari, and R. M. Pattabi, "Enhancing the photocatalytic efficiency of cds nanostructures by zns: A case study on the degradation of methylene blue," *Mater. Today: Proc.*, 2023.

[31] P. Huo et al., "Incorporation of n–zno/cds/graphene oxide composite photocatalyst for enhanced photocatalytic activity under visible light," *J. Alloy. Compd.*, vol. 670, pp. 198–209, 2016.

[32] K. Wu, Z. Chen, H. Lv, H. Zhu, C. L. Hill, and T. Lian, "Hole removal rate limits photodriven h2 generation efficiency in cds-pt and cdse/cds-pt semiconductor nanorod–metal tip heterostructures," *J. Am. Chem. Soc.*, vol. 136, no. 21, pp. 7708–7716, 2014.

[33] M. Alomar, Y. Liu, W. Chen, and H. Fida, "Controlling the growth of ultrathin mos2 nanosheets/cds nanoparticles by two-step solvothermal synthesis for enhancing photocatalytic activities under visible light," *Appl. Surf. Sci.*, vol. 480, pp. 1078–1088, 2019.

[34] A. V. Isarov and J. Chrysochoos, "Optical and photochemical properties of nonstoichiometric cadmium sulfide nanoparticles: Surface modification with copper (ii) ions," *Langmuir*, vol. 13, no. 12, pp. 3142–3149, 1997.

[35] B. Małecka, "Thermal decomposition of cd(ch3coo)2·2h2o studied by a coupled tg-dta-ms method," *J. Therm. Anal. Calorim.*, vol. 78, no. 2, pp. 535–544, 2004.

[36] E. Lizarraga, C. Zabaleta, and J. Palop, "Mechanism of thermal decomposition of thiourea derivatives," *J. Therm. Anal. Calorim.*, vol. 93, no. 3, pp. 887–898, 2008.

[37] F. Vaquero, J. L. G. Fierro, and R. M. Navarro Yerga, "From nanorods to nanowires of cds synthesized by a solvothermal method: Influence of the morphology on the photoactivity for hydrogen evolution from water," *Molecules*, vol. 21, no. 4, p. 401, 2016.

[38] T. Senasu, K. Hemavibool, and S. Nanan, "Hydrothermally grown cds nanoparticles for photodegradation of anionic azo dyes under uv-visible light irradiation," *RSC Adv.*, vol. 8, no. 40, pp. 22 592–22 605, 2018.

[39] R. Atchudan et al., "Sustainable synthesis of multi-functional carbon dots as optical nanoprobe for selective sensing of heavy metal ions," *J. Taiwan Inst. Chem. Eng.*, vol. 165, p. 105 770, 2024.

[40] A. Z. Shaikh, S. D. Satpute, J. R. Gadde, R. R. Hawaldar, and K. C. Mohite, "Influence of chemical bath deposition temperatures on cadmium sulphide thin film and photosensor application," *ES Mater. & Manuf.*, vol. 20, no. 2, p. 819, 2023.

[41] Y. Wang et al., "Effect of sulfur source on photocatalytic degradation performance of cds/mos2 prepared with one-step hydrothermal synthesis," *J. Environ. Sci.*, vol. 65, pp. 347–355, 2018.

[42] B. M. Al-Maswari et al., "Synthesis of perovskite bismuth ferrite embedded nitrogen-doped carbon (bifeo3-nc) nanocomposite for energy storage application," *J. Energy Storage*, vol. 44, p. 103 515, 2021.

[43] M. Dwivedi, V. Tripathi, D. Kumar, and D. K. Gupta, "Structural and morphological characterization of cds nanoparticles," *Curr. Phys. Chem.*, vol. 11, no. 1, pp. 69–79, 2021.

[44] X. Chen et al., "Multi-pathway photoelectron migration in globular flower-like in2o3/agbr/bi2wo6 synthesized by microwave-assisted method with enhanced photocatalytic activity," *J. Mol. Catal. A: Chem.*, vol. 414, pp. 27–36, 2016.

[45] X. Zhou, J. Huang, H. Zhang, H. Sun, and W. Tu, "Controlled synthesis of cds nanoparticles and their surface loading with mos2 for hydrogen evolution under visible light," *Int. J. Hydrog. Energy*, vol. 41, no. 33, pp. 14 758–14 767, 2016.

[46] A. Abdulkarem, A. Aref, A. Abdulhabeeb, Y.-F. Li, and Y. Yu, "Synthesis of bi2o3/cu2o nanoflowers by hydrothermal method and its photocatalytic activity enhancement under simulated sunlight," *J. Alloy. Compd.*, vol. 560, pp. 132–141, 2013.

[47] A. Al-Muntaser et al., "Fabrication and characterizations of nanocomposite flexible films of zno and polyvinyl chloride/poly (n-vinyl carbazole) polymers for dielectric capacitors," *Arab. J. Chem.*, vol. 16, no. 10, p. 105 171, 2023.